Trace Water in Lead Iodide Affecting Perovskite Crystal Nucleation Limits the Performance of Perovskite Solar Cells

Renjun Guo, Qiu Xiong, Aleksander Ulatowski, Saisai Li, Zijin Ding, Tianxiao Xiao, Suzhe Liang, Julian E. Heger, Tianfu Guan, Xinyu Jiang, Kun Sun, Lennart K. Reb, Manuel A. Reus, Andrei Chumakov, Matthias Schwartzkopf, Minjian Yuan, Yi Hou, Stephan V. Roth, Laura M. Herz, Peng Gao,* and Peter Müller-Buschbaum*

The experimental replicability of highly efficient perovskite solar cells (PSCs) is a persistent challenge faced by laboratories worldwide. Although trace impurities in raw materials can impact the experimental reproducibility of high-performance PSCs, the in situ study of how trace impurities affect perovskite film growth is never investigated. Here, light is shed on the impact of inevitable water contamination in lead iodide (PbI_2) on the replicability of device performance, mainly depending on the synthesis methods of PbI_2. Through synchrotron-based structure characterization, it is uncovered that even slight additions of water to PbI_2 accelerate the crystallization process in the perovskite layer during annealing. However, this accelerated crystallization also results in an imbalance of charge-carrier mobilities, leading to a degradation in device performance and reduced longevity of the solar cells. It is also found that anhydrous PbI_2 promotes a homogenous nucleation process and improves perovskite film growth. Finally, the PSCs achieve a remarkable certified power conversion efficiency of 24.3%. This breakthrough demonstrates the significance of understanding and precisely managing the water content in PbI_2 to ensure the experimental replicability of high-efficiency PSCs.

1. Introduction

A tunable bandgap, low crystal formation energy, and high defect tolerance make metal halide perovskite materials ideal candidates for wide-range optoelectronic applications such as solar cells, light-emitting diodes, and photodetectors.[1–3] Moreover, the advantage of low cost due to solution-based processing and economically abundant materials further makes perovskite solar cells (PSCs) a promising renewable energy technology for large-scale applications to meet the challenge of the energy crisis.[4] Through diligent research and intensive collaboration at a world level, PSCs have achieved performance comparable to that of silicon solar cells.[5] Device engineering progress, such as the sequential solution deposition method, solvent engineering, and compositional engineering, help achieve power conversion efficiencies (PCEs) above 20%.[6–8] Furthermore, trap management through surface/bulk passivation and interfacial engineering has boosted the certified performance of PSCs to 26.1%.[9,10] However, the experimental replicability in different labs for achieving highly efficient PSCs is a nagging challenge in the field, and only a few groups worldwide can obtain devices with a certified PCE > 24%. Thus, the fundamental limitations to experimental replicability during the fabrication process of highly efficient PSCs have emerged as one of the most pressing subjects requiring urgent investigation.

R. Guo, T. Xiao, S. Liang, J. E. Heger, T. Guan, X. Jiang, K. Sun, L. K. Reb, M. A. Reus
Department of Physics, Chair for Functional Materials, TUM School of Natural Sciences
Technical University of Munich
85748 Garching, Germany

R. Guo, Y. Hou
Solar Energy Research Institute of Singapore
National University of Singapore
117574 Singapore, Singapore

Q. Xiong, P. Gao
Fujian Institute of Research on the Structure of Matter
Chinese Academy of Sciences
350002 Fuzhou, China
E-mail: peng.gao@fjirsm.ac.cn

A. Ulatowski, L. M. Herz
Department of Physics
University of Oxford
Clarendon Laboratory
OX13PU Oxford, UK

**ADVANCED
SCIENCE NEWS**

www.advancedsciencenews.com

**ADVANCED
MATERIALS**

www.advmat.de

Various parameters limit the experimental replicability of the device fabrication process: i) material purity;[11–15] ii) divergent fabrication pathways, e.g., mixing methods of precursor materials (such as a mixture of raw chemicals or a mixture of perovskite single-crystal powder;[16] and iii) sensitive processing windows, e.g., lower relative humidity atmosphere (<20%).[17] To achieve ideal optoelectronic properties, it is necessary to consider the impacts of impurities on performance. For example, a study by Wakamiya et al. showed that a dehydration process for lead iodide (PbI_2) could double the total performance of PSCs.[11] Furthermore, a study found that water as a minute constituent in N,N-dimethylformamide (DMF) or dimethyl sulfoxide (DMSO) actively participates in the whole perovskite formation scheme.[18] Water could also exert beneficial or detrimental effects on device fabrication and stability.[19–22] However, the primary synthesis method of PbI_2 ("golden rain" reaction) is water-based and restricts the possibility of a highly dehydrated process. All solvents, e.g., DMF, DMSO, and Iso-propanol (IPA) for perovskite-related precursors, are highly hygroscopic. Previous studies have confirmed that suitable water in DMF or IPA for sequential deposition methods could be beneficial for device performance due to the suppression of pinholes.[20,23] All previous studies focus on how the humidity in the air during the annealing process affects device performance and crystallization and overlook the impact of intermolecular engineering through DMSO in the sequential fabrication method.[24–28] Sequential fabrication methods open a new avenue for improving the performance of PSCs, leading to many world-record PCEs of PSCs.[29,30] In addition, as seen in thermodynamic calculations, water could intercalate with methylammonium lead halide perovskite materials and form monohydrated phases. This further causes the favorable formation of a PbI_2 vacancy complex, creating a deep charge transition level and enhance nonradiative recombination processes.[22,31,32]

However, the relative fundamental mechanisms have yet to be investigated. To close this knowledge gap, we report that the water content of PbI_2 is one of the most critical parameters limiting the reproducibility and performance of PSCs. We reveal that an increasing amount of trace water in PbI_2 leads to a heterogeneous crystallization process and worsens the texture of PbI_2 in lead halide perovskite films. The stability constants of lead halide perovskite complexes in the precursor decrease with an increasing amount of water in the PbI_2 precursor, which drives different crystallization and texture formation processes. We demonstrate that the hole mobility decreases because the scattering rate of holes from defects increases with increasing water content in the PbI_2. The strong imbalance between the hole and electron mobilities in high-water-content films restricts the device performance. Finally, through fine control (<15 ppm) of the trace-water content in PbI_2, we achieved a certified 24.3% PCE for solar cells with an aperture area of 0.095 cm^2. Moreover, we applied the same strategy for large-aperture-area solar cells and reached a certified PCE of 22.9% for an aperture area of 1 cm^2, demonstrating the high uniformity of PSCs.

2. Results

2.1. Different Synthesis Methods of PbI_2 Precursor and Relative Performance of Perovskite Solar Cells

We first screen the effects of different synthesis methods of PbI_2 purchased from companies on the device performance. The "golden rain reaction" is a mainstream solution-process-based PbI_2 synthesis method (type I in **Figure 1a-I**). The water content can reach 50 ppm in this reaction due to the water-based synthesis method (Table S1, Supporting Information).[11] By contrast, direct synthesis of PbI_2 at high temperatures (type II in Figure 1a-II) could make the PbI_2 an anhydrous level.[13] As seen in Figure 1b, the increasing water content in PbI_2 harms the device performance by reducing the open-circuit voltage (V_{OC}), short-circuit current (J_{SC}), and PCE. Through fabricating PSCs by the one-step antisolvent method with the components of $(MAPbBr_3)_{0.17}(FAPbI_3)_{0.83}$, we confirm that the adverse effects of higher water content in PbI_2 on device performance are independent of perovskite components and fabrication methods (Figure S1, Supporting Information).[7] Although type II PbI_2 could deliver PSCs with higher performance, the price of type I PbI_2 is much higher than that of type II (Table S1, Supporting Information). To avoid the effects of other impurities, e.g., acetate and nitrate, we design an experiment by adding deionized (DI) water in type II PbI_2 prepared precursor for the following investigations.[14,15]

2.2. Effect of Water Content in Lead Iodide Precursor on the Growth of $MA_xFA_{1-x}PbI_3$ ($x < 0.05$) Perovskite Films

Synchrotron-based grazing-incidence wide-angle X-ray scattering (GIWAXS) is utilized to explore the effects of water content in PbI_2 on perovskite crystallization.[33–35] We actively introduced different amounts of deionized water into the type II PbI_2 prepared precursor because of its anhydrous feature. Then, we used a sequential deposition method to fabricate the perovskite layer and monitored the annealing process of the perovskite layer

S. Li, Z. Ding, M. Yuan
Department of Chemistry
Nankai University
300071 Tianjin, China
A. Chumakov, M. Schwartzkopf, S. V. Roth
Deutsches Elektronen-Synchrotron
Notkestrasse 85, 22607 Hamburg, Germany
Y. Hou
Chemical and Biomolecular Engineering
National University of Singapore
117585 Singapore, Singapore
S. V. Roth
Department of Fiber and Polymer Technology
KTH Royal Institute of Technology
10044 Stockholm, Sweden
L. M. Herz
Institute for Advanced Study
Technical University of Munich
85748 Garching, Germany
P. Müller-Buschbaum
Heinz Maier-Leibnitz-Zentrum
Technical University of Munich
85748 Garching, Germany
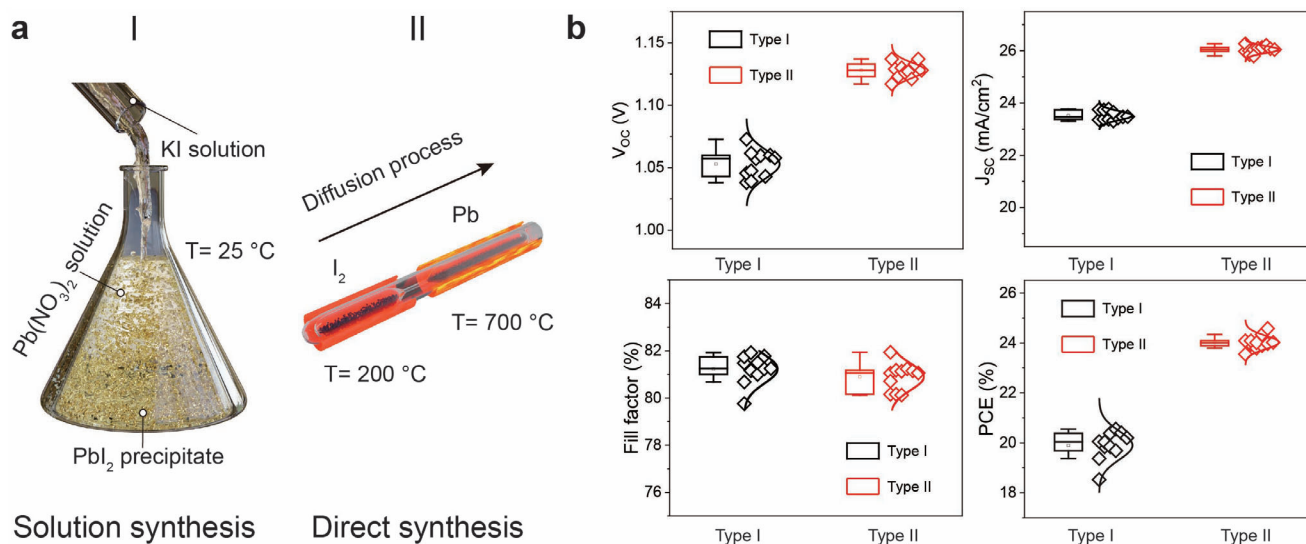E-mail: muellerb@ph.tum.de

Figure 1. Different synthesis methods of PbI$_2$ precursor and relative performance of perovskite solar cells. a) Schematic diagram of water solution-based PbI$_2$ synthesis (labeled "Type I") for which potassium iodide and lead(II) nitrate are dissolved in water separately, and these two transport solvents are mixed in the vessel with a heating process. After cooling down at room temperature, the yellow precipitate of lead iodide appears. For the direct synthesis (labeled "Type II"), an ampule made from quartz glass is divided into two parts, with the elements separately placed in the solid phase, iodine in small balls and lead in small wire pieces. Then, the ampule is inserted in a resistance furnace with two temperature regions; the iodide part is heated to 150 °C and the lead part to 700 °C. Lead diffuses slowly in the lead part and reacts with the melted lead. b) Performance statistics of solar cells with the perovskite component of MA$_x$FA$_{1-x}$PbI$_3$ ($x < 0.05$) as active layer fabricated by type I (<100 ppm) and type II PbI$_2$ (<15 ppm), shown in box-and-whisker plots (center line, average; box limit, standard deviation; whiskers, outliers of 11 devices).

at 150 °C with relative humidity (35 ± 1%) in air.[30] The time evolution of 2D GIWAXS data is plotted as a line profile integration in which the crystallization process can be analyzed (**Figure 2a** and Figure S2–S5 (Supporting Information)). We observed that the perovskite phase forms before annealing with unreacted perovskite intermediate phases. An additional amount of water (from 0 to 7000 ppm, Note S1, Supporting Information) in the perovskite films consumes orthorhombic complexes (MA$_x$FA$_{1-x}$)$_2$(Pb$_3$I$_8$)·2DMSO (space group $Cmc2_1$) (q = 4.7, 5.1, 6.5 nm^{-1}) much faster during the annealing process.[36–38] We note that 0 ppm only refers to the water content we add to the PbI$_2$ precursor, which does not mean the actual water content in the precursor. Furthermore, the reaction time of these complexes during the annealing process decreased from 600 to 50 s with an increasing amount of water, which causes both the reaction of the complexes and faster formation of the PbI$_2$ phase (q = 9.0 nm^{-1}) in the perovskite films. Through a detailed analysis of the perovskite intermediate phase (q = 6.5 nm^{-1}) using the Jeziorny equation (Figure 2b and Figure S6, Note S2, and Table S4 (Supporting Information)), the lower n values extracted from perovskite films fabricated by PbI$_2$ precursors with higher water contents indicate that the increasing water content may cause the heterogeneous dominated nucleation of the perovskite intermediate phases as abovementioned.[39–41]

Scanning electron microscopy (SEM) images offer direct evidence for nucleation. The obtained SEM images confirm the appearance of heterogeneous-dominated nucleation (Figure 2c). The increasing water content leads to a competing mechanism between heterogeneous and homogenous nucleation for perovskite intermediate phases due to the binding competition between DMSO and H$_2$O. Also, we notice that the heteroge-

neous dominated nucleation also causes an absence of a PbI$_2$ phase at the surface of the perovskite layer, which could be detrimental given that previous reports have indicated that excess PbI$_2$ aids performance (Figure S7, Supporting Information).[9,42] The surface area that contributes to the growth of the nucleus is high in homogeneous nucleation, leading to a higher possibility for the decomposition of perovskite films to PbI$_2$.[43] We also investigated the azimuthal integration of the 2D GIWAXS data for the PbI$_2$ phase (space group $P63mc$) at q = 17.9 nm^{-1}, and we noted a noticeable decrease in the intensity of the PbI$_2$ texture (Figure 2d and Figure S8 (Supporting Information)). This finding implies the formation of weaker textures for PbI$_2$. This texture could affect the device performance, according to previous studies.[44] Furthermore, it is essential to note that varying amounts of water content in PbI$_2$ precursors substantially influence the morphology of PbI$_2$ films. All PbI$_2$ precursors are filtered before the preparation of PbI$_2$ films. As water content increases, we observe that the grain size of films increases, which might be related to the weaker coordination process with DMSO (as shown in Figures S9,S10 in the Supporting Information).

To examine the intrinsic driving force of the immediate consumption of perovskite-related complexes in the perovskite film, we used the continuous variation method for signifying the stability constant of the PbI$_2$·DMSO complex (Figure S11 and Note S3, Supporting Information).[45] The increasing amount of water in the PbI$_2$ precursor can dramatically decrease the stability constant of complexes, resulting in a suspension of PbI$_2$ particles (Figure 2e). This phenomenon suggests that water has a lower hydrogen-bond accepting ability than DMF or DMSO in perovskite intermediate complexes. The decreasing
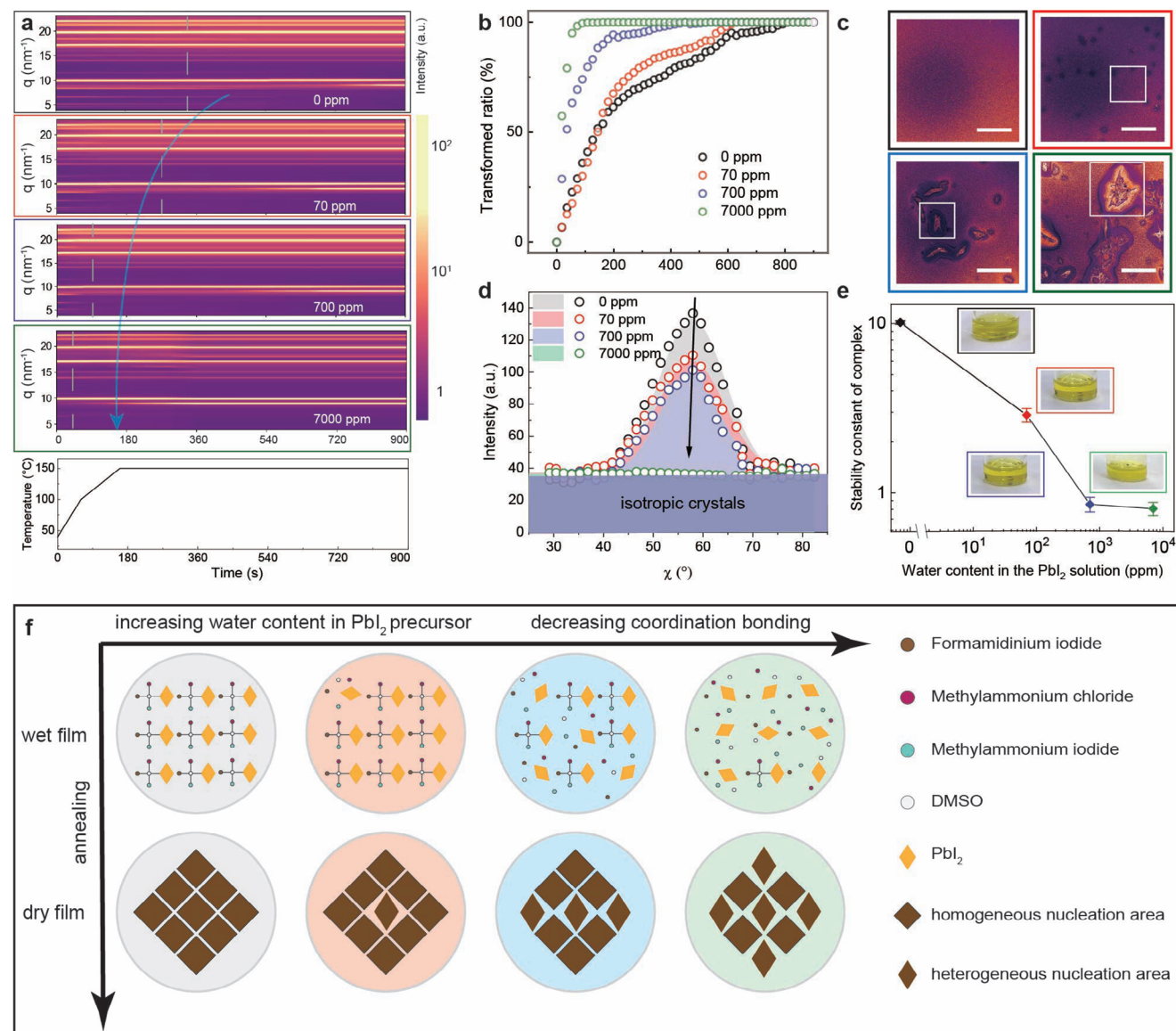
Figure 2. Effect of water content in lead iodide precursor on the growth of $MA_xFA_{1-x}PbI_3$ ($x < 0.05$) perovskite films. a) Time evolution of synchrotron-radiation-based GIWAXS data plotted as radially integrated line profiles of 2D GIWAXS data during the annealing process of perovskite films with different water contents: 0 ppm water (black frame), 70 ppm water (red frame), 700 ppm water (blue frame), 7000 ppm water (green frame). b) The transformed ratio of orthorhombic complexes $(MA_xFA_{1-x})_2(Pb_3I_8)\cdot 2DMSO$ at $q = 6.5$ nm^{-1} for static perovskite films after annealing with different water contents and the initial peak density of this complex at the beginning of annealing process is defined as the zero-fraction transformation point. c) SEM images for $MA_xFA_{1-x}PbI_3$ ($x < 0.05$) perovskite films with 0 ppm water (black frame), 70 ppm water (red frame), 700 ppm water (blue frame), 7000 ppm water (green frame), and the scale bar is 200 μm. d) Texture changes of the PbI_2 phase at $q = 18.4$ nm^{-1} in perovskite films with different water contents. e) The stability constant of PbI_2 solutions for different amounts of water and the inset photos are PbI_2 solution in DMF and DMSO (volume ratio = 9.5:0.5) with varying amounts of water. f) Schematic diagram of how other water contents in the PbI_2 precursor affect the perovskite crystal formation. The gray, red, blue, and green circles indicate 0, 70, 700, and 7000 ppm water. An increasing amount of water in wet film breaks the coordination bonding between PbI_2 and DMSO, which could cause a heterogeneous dominated nucleation area for the dry perovskite film after the annealing process.

amount of perovskite-related complexes is related to the loss of $PbI_2\cdot DMSO$ in the films and causes a fast reaction of the complexes during the annealing process of the perovskite films.[18] As shown in Figure 2f, the coordination bonding of $PbI_2\cdot DMSO$ complexes is stable when the PbI_2 film's water content is low. This leads to a slower crystallization for the PbI_2 phase, which develops a stronger texture during the annealing process.

By contrast, increasing water content breaks the coordination bonding between the $PbI_2\cdot DMSO$ complexes owing to a lower stability constant. The weaker coordination causes faster crystallization and randomly oriented PbI_2 phases. The in situ GIWAXS experiments of annealing PbI_2 films with different amounts of water confirm our assumptions (Figure S12, Supporting Information). Pseudo-X-ray-diffraction (XRD) results obtained from 2D GIWAXS data demonstrate that, without adding water to the
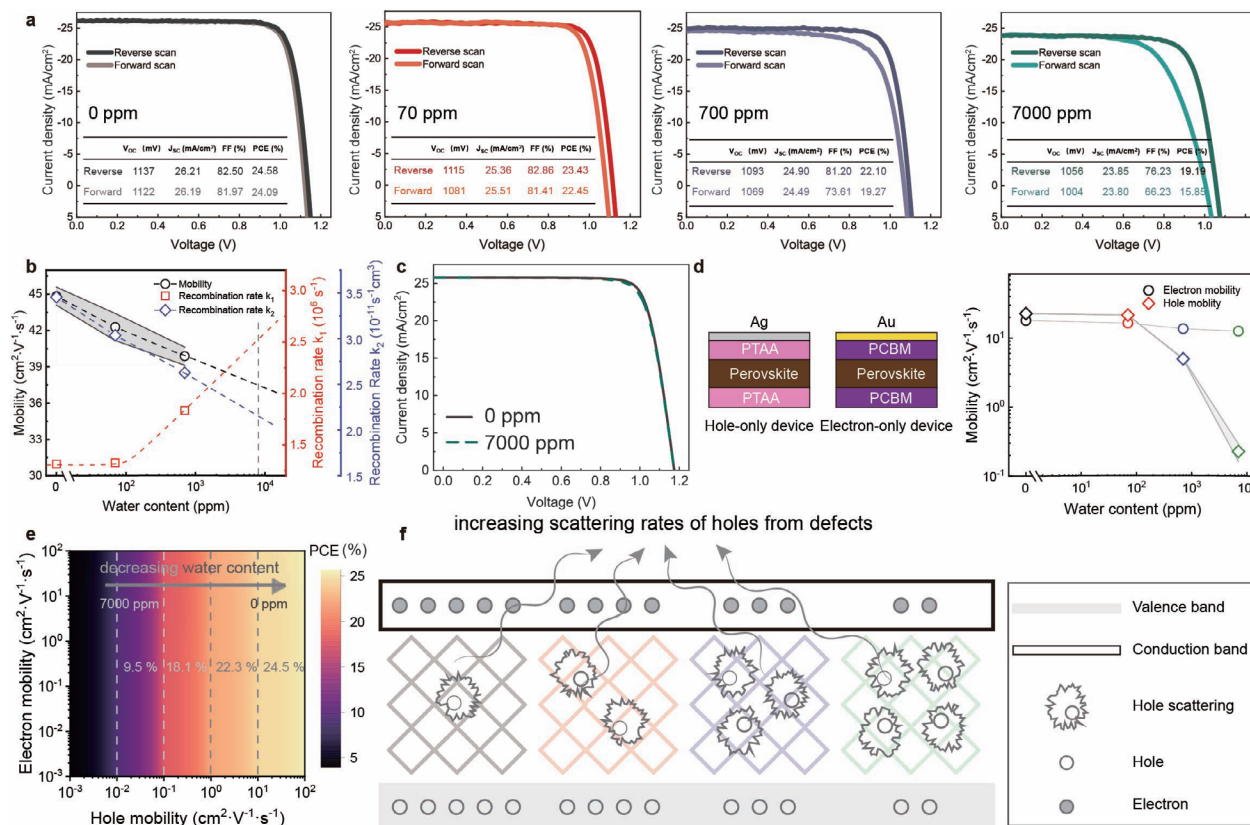
**ADVANCED
SCIENCE NEWS**

www.advancedsciencenews.com

**ADVANCED
MATERIALS**

www.advmat.de

Figure 3. Effect of water content in PbI$_2$ precursor on the performance of solar cells. a) The version of MA$_x$FA$_{1-x}$PbI$_3$ ($x < 0.05$) solar cells with 0, 70, 70, and 7000 ppm water in PbI$_2$ precursors. b) Electron–hole sum mobilities, trap-assistant recombination rates, and bimolecular recombination rate constants extracted from modeling OPTP and TRPL spectra for different amounts of water in the perovskite layer. c) Simulated J–V curves with modifying recombination rates subtracted from the perovskite films fabricated by different amounts of water in the PbI$_2$ precursor: 0 (solid black line) and 7000 (green dashed line). d) Schemes of applied hole-only and electron-only devices for measuring hole and electron mobilities separately obtained from space-charge limited current measurements. e) Modeled dependence of PCE for solar cells with different electron and hole mobilities extracted from "drift–diffusion" simulations, suggesting that increasing water contents leads to a decrease in hole mobilities and associated worsening device performance. f) Schematic indicating increasing scattering rates of holes arising from an increased density of defects deriving from rising water content in the perovskite films: 0 (gray), 70 ppm (red), 700 ppm (blue), 7000 ppm (green).

PbI$_2$ film, the annealed PbI$_2$ film presents the pure phase formation of PbI$_2$·DMSO (space group, *Pnam*). Water addition at 70 and 700 ppm to the lead iodide precursors suppresses the construction of such a phase (Figure S13, Supporting Information). Water addition at 7000 ppm even drives PbI$_2$·DMF (space group, *Pnam*) formation, which causes the heterogeneous dominated growth of perovskite films (Figure S7, Supporting Information). To validate the general applicability of our assumption to mainstream perovskite fabrication methods, we conducted further investigations on the effects of water content in one-step perovskite fabrication using different solvents by adding the same amount of DI water in perovskite precursors (DMSO and *N*-methyl-2-pyrrolidone). This study targeted world-record efficiency and upscaling fabrication processes (Figure S14, Supporting Information). Our findings revealed that similar to the two-step method, the perovskite intermediate complexes also disappear in the wet perovskite films as water content increases. This consistency in results across different fabrication methods supports the validity of our assumption. Finally, weaker perovskite intermediate complexes result in a more pronounced delta perovskite phase and a diminished face-on perovskite (100) orien-

tation, potentially influencing charge transfer processes in the PSCs.

2.3. Effect of Water Content in PbI$_2$ Precursor on the Performance of Solar Cells

To assess the effects of water content in PbI$_2$, we fabricated devices with different water contents in PbI$_2$ precursors. **Figure 3a** shows that the device performance declines with increasing water in the PbI$_2$ precursor. Increasing the water concentration in the PbI$_2$ precursor causes a decrease in the average PCE of 18.2% from the original PCE of 24.0%. By using the anhydrous PbI$_2$, we achieved a certified PCE of 24.3% with a small aperture area and a certified PCE of 22.9% with a large aperture area (Figures S15,S16, Supporting Information). The certified processes are similar to recent published results. The detailed device statistics and the external quantum efficiency spectra are shown in Figures S17,S18 (Supporting Information). The stabilized PCE is one critical evaluation of PSCs, and we achieve a stabilized PCE of 24.48% with a 400 s maximum-power-point tracking (MPPT)

scan (Figure S19, Supporting Information). A previous study has shown that the water content in PbI$_2$ may affect the optoelectronic properties of the PbI$_2$ film. Thus, the optoelectronic properties of perovskite films made of PbI$_2$ with different water contents must be investigated.

We revealed the charge-carrier dynamics of MA$_x$FA$_{1-x}$PbI$_3$ ($x < 0.05$) perovskite layers fabricated with different amounts of water in the PbI$_2$ precursor through optical-pump THz-probe (OPTP) spectroscopy and time-resolved photoluminescence (TRPL) spectra.[46,47] Figure 3b demonstrates clearly that the optoelectronic properties of the films decline substantially as the water content in the PbI$_2$ precursor increases. The charge-carrier sum mobility reduces from 44.84 cm^2 V^{-1} s^{-1} (0 ppm) to 39.88 cm^2 V^{-1} s^{-1} (700 ppm), which will worsen the device performance (Note S4 and Figure S20, Supporting Information). Meanwhile, we observed a reduced bimolecular recombination rate constant with the higher water content film (a decrease from 3.45×10^{-11} to 2.62×10^{-11} s^{-1} cm^3) from 0 to 700 ppm owing to changes in photon recycling effects induced by the morphological changes which will impact light outcoupling (Note S5, Supporting Information). In addition, TRPL transients derived from the time-correlated single-photon counting (TCSPC) technique demonstrate more robust trap-assisted charge-carrier recombination rates in case of higher water contents in the perovskite films (Figure S21, Supporting Information), which increases from 1.31×10^6 to 1.83×10^6 s^{-1} (Note S5, Supporting Information). We found that the high roughness of the perovskite film with 7000 ppm water yielded an undetectable signal for the OPTP spectroscopy (Figure S22, Supporting Information); therefore, the lines in Figure 3b indicate linear extrapolation to predict the evolution for the highest water-content level.

To quantify the effects of charge-carrier dynamics on device performance, we use the "drift–diffusion" model through Solar Cell Capacitance Simulator-One Dimension (SCAPS-1D) to simulate the efficiency of solar cells.[48] We first assess the effects of increasing trap-assisted recombination rates related to higher trap densities and decreasing radiative bimolecular recombination rates associated with lower photon retention (Note S7, Supporting Information). Then, by quantifying charge-carrier and trap densities, we modify the trap densities, radiative recombination coefficients, and charge-carrier mobilities in the "drift–diffusion" model (Note S8 and Tables S5–S8, Supporting Information). The results show a minor reduction in device performance with increased trap-assisted recombination rates and decreased bimolecular recombination rates (Figure 3c). Due to the substantial mismatches between experiment and simulation results, we propose that a severe reduction of device performance with increasing water content in the perovskite may arise from the introduction of imbalanced hole and electron mobilities, which cannot be directly disentangled by OPTP spectroscopy owing to its limitation of measuring combined sum-electron–hole mobilities.[49] Also, Solanki et al. reported that a proper amount of heavy water could boost the device performance using one-step antisolvent methods due to enhanced charge carrier diffusion lengths and water presenting a different interaction mechanism than D$_2$O.[50] These results motivate us to figure out the detailed charge-carrier dynamics.

We use space-charge limited current measurements to confirm this proposed efficiency loss mechanism to separate the

hole and electron mobilities (Note S8, Figure S23, and Table S8, Supporting Information).[3,51] Through the application of hole-only and electron-only architectures for the devices, as shown in Figure 3d, we indeed find that the hole mobilities decrease from 22.64 to 0.23 cm^2 V^{-1} s^{-1} for the fabricated perovskite devices with an increasing amount of water in PbI$_2$ precursors from 0 to 7000 ppm. In comparison, the electron mobilities increase from 17.95 to 12.59 cm^2 V^{-1} s^{-1}. Furthermore, by simulating the array among different hole and electron mobilities for device performance (Figure 3e and Figure S24 (Supporting Information)), we demonstrate how the imbalanced hole and electron mobilities in perovskite films fabricated from PbI$_2$ precursors with higher water content lead to severe reduction in device performance. Thus, the lower hole mobility strongly restricts the optoelectronic properties of the perovskite layer, caused by increased scattering rates of holes from defects, as evident from the rising trap-related recombination rate k_1 (Figure 3f).[52] The dramatic decrease of hole mobility might correlate to an absence of a PbI$_2$ phase at the surface of the perovskite layer (Figure S7, Supporting Information) and the weaker PbI$_2$ texture at $q = 17.9$ nm^{-1} (Figure 2d and Figure S8 (Supporting Information)). In addition, we employed thermal admittance spectroscopy (TAS) analysis to quantify the reduction of trap states in perovskite films (Figure S25, Supporting Information). Our findings consistently demonstrate a marked increase in the trap density of states, affecting both shallow and deep trap states, as a result of the rising water content in PbI$_2$. This enhancement in trap density of states within the perovskite materials underscores the critical role of water content in influencing the electronic properties of the perovskite film.[53]

2.4. Effects of Water Content on the Operational Stability of Solar Cells

To assess performance under real-world conditions, evaluating PSCs' operational stability under MPPT conditions is critical. Thus, we explored the effects of water contents in PbI$_2$ on the long-term operational stability of the perovskite solar cells (**Figure 4**). We aged PSCs fabricated with PbI$_2$ precursors of different water contents, as shown in Figure 4a–d, with the International Summit on Organic Photovoltaci Stability (ISOS)-L-2 (1 sun, 55 °C, nitrogen) protocol under MPPT conditions. The PSCs fabricated with more water content in the PbI$_2$ precursor suffered a much more rapid performance loss within the 390 h operation. Interestingly, the excess PbI$_2$ in the perovskite film causes all PSCs to show a performance loss at the beginning stage of MPPT, after which performance remains relatively stable.[9] We also examine that different water contents in PbI$_2$ do not affect the intrinsic moisture stability of perovskite films (Figure S26, Supporting Information).

To accurately evaluate the intrinsic device operational stability fabricated by the daily used PbI$_2$ in the lab. We also manufacture PSCs with type I (solution synthesis) and type II PbI$_2$ (high-temperature synthesis) to investigate their intrinsic operational stability by avoiding temperature effects and age them with the ISOS-L-1 (1 sun, 25 °C, encapsulation) protocol under MPPT conditions. Devices fabricated from the type I PbI$_2$ show a 60% relative efficiency decrease after 350 h of continuous operation (Figure 4e), while those manufactured from type II PbI$_2$ present
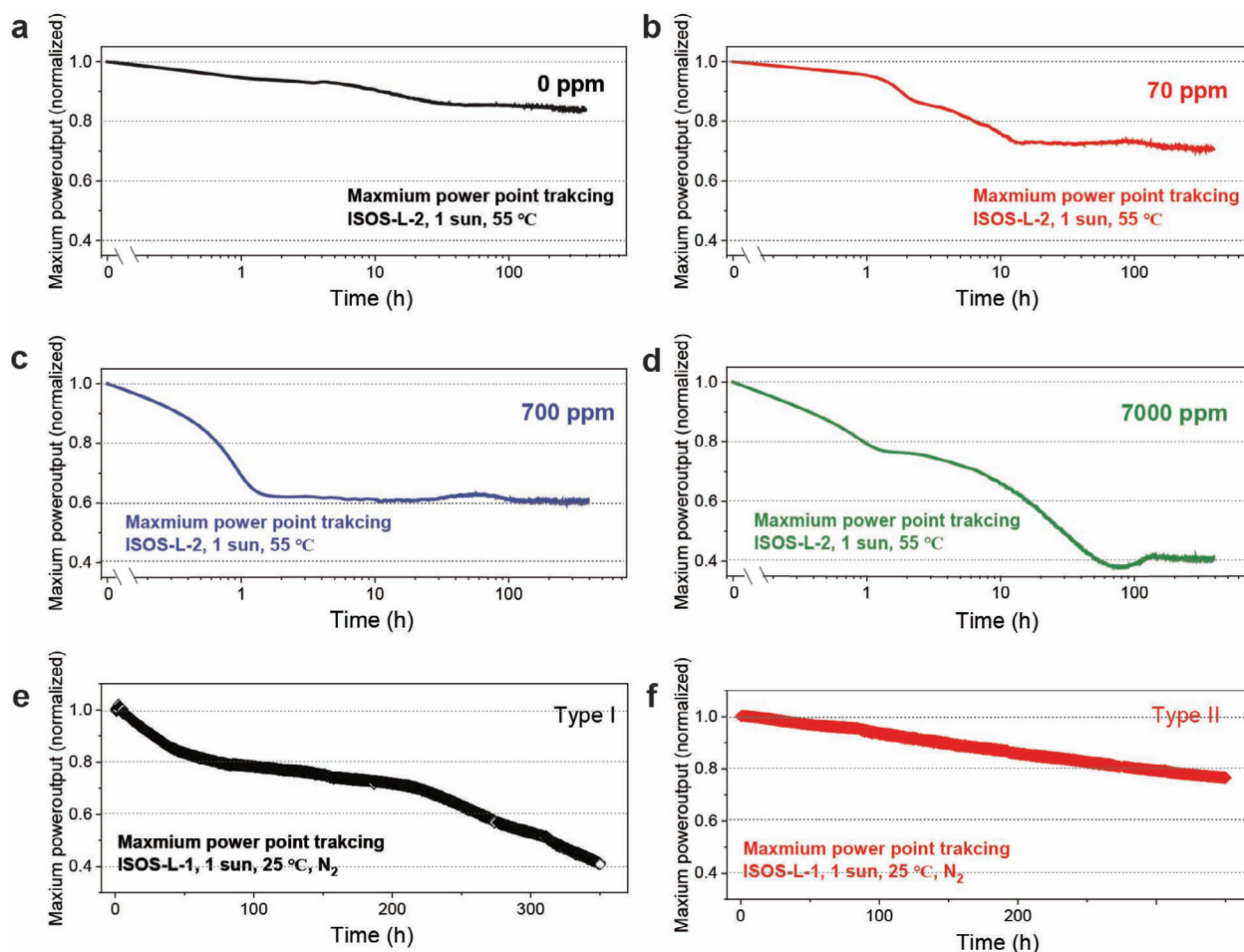
**ADVANCED
SCIENCE NEWS**
www.advancedsciencenews.com

**ADVANCED
MATERIALS**
www.advmat.de

Figure 4. Effects of water content on the operational stability of solar cells. Operational stability of PSCs with $MA_xFA_{1-x}PbI_3$ ($x < 0.05$) active layers fabricated with PbI_2 precursors containing different water contents, a) 0 ppm, b) 70 ppm, c) 700 ppm, and d) 7000 ppm. All PSCs were recorded under the ISOS-L-2 protocol by the maximum power point tracking method for encapsulated devices in air and continuous one-sun illumination at ≈55 °C. Operational stability of perovskite solar cells fabricated with e) type I and f) type II PbI_2 under the ISOS-L-1 protocol (maximum power point tracking, in N_2, continuous one-sun illumination at ≈25 °C). A total of six individual pixels are connected in series for all MPPT measurements.

only about 20% relative performance loss after a 350 h procedure (Figure 4f). These results highlight that trace water contamination in the PbI_2 precursor not only deteriorates performance but also worsens the operational stability of photovoltaic devices.

3. Conclusion

Overall, our findings thus reveal that paying close attention to unintended water contamination in PbI_2 precursors is vital to reliable, high-efficiency device performance and, most importantly, the operational stability of perovskite-based solar cells. Anhydrous reagents, solvents, and materials could enhance device performance. However, a careful analysis from perspectives of cost-benefit analysis, industrialization potential, and technical advancements should be conducted before applying different fabrication technologies of PSCs. Furthermore, we should develop potential strategies or alternative approaches to mitigate the cost increase and make the perovskite preparation more economically competitive, which could balance the fabrication cost, device performance, and longevity.

4. Experimental Section

Materials: Patterned Indium Tin Oxide (ITO) glass substrates were purchased from Yingkou Shangneng Photoelectric Material Co., Ltd., China. Fluoride Tin Oxide (FTO) glass substrates (T18VU70, 12–13 Ω □$^{-1}$, 10–20% Haze for small area devices, and A22-8A, 8 Ω □$^{-1}$, 11% Haze for large area devices, respectively) were provided from Asahi, China. The tin(IV) oxide 15% in H_2O colloidal dispersion was purchased from Alfa Aesar (product number: 44592). Methylammonium iodide (MAI, anhydrous, product number: MI-0-99-9), formamidinium iodide (FAI, anhydrous, product number: FI-0-99-9), methylammonium chloride (MACl, anhydrous, MC-0-99-9) were purchase Greatcellsolar Italy as the anhydrous level. Lead iodides were purchased from two different companies separately. Hellmanex III (product number: Z805939-1EA), DMF (anhydrous, product number: 227056), DMSO (anhydrous, product number: 276855), 2-propanol (anhydrous, product number: 278475), chlorobenzene (CB, anhydrous, product number: 284513), Lithum bis(trifluoromethanesulfonyl)imide (Li-TFSI) (product number: 544094), acetonitrile (product number: 2710004), 4-*tert*-butylpyridine (product number: 142379), 2,2',7,7'-Tetrakis[N,N-di(4-methoxyphenyl)amino]-9,9'-spirobifluorenen (spiro-OMeTAD) (product number: 902500), poly[bis(4-phenyl)(2,4,6-trimethylphenyl)amine], poly(triaryl amine) (PTAA, product number: 702471) were purchased from Sigma-Aldrich. Phenyl-C61-butyric

**ADVANCED
SCIENCE NEWS**

www.advancedsciencenews.com

**ADVANCED
MATERIALS**

www.advmat.de

acid methyl ester (PCBM, product number: 060995) was purchased from Solenne BV (stop production).

Device Fabrication: FTO or ITO glass substrates were cleaned sequentially through a diluted Hellmanex III (2:98 volume ratio in the DI water), DI water, acetone, isopropanol, and ethanol for 15 min under an ultrasonic bath. Then, a diluted SnO_2 solution (1:4 volume ratio in DI water) was spin-coated (3000 rpm for 30 s) on oxygen-plasma cleaned substrates (160 W, 15 min) with a postannealing at 150 °C for 30 min. Next, substrates were transferred to a nitrogen-filled glove box.

Two-Step Fabrication: 691.5 mg PbI_2 was stirred in a mixed DMF:DMSO (950:50 μL) solution at 70 °C for 6 h. Then, 0.1, 1, and 10 μL DI water was added to the PbI_2 solution. After that, different PbI_2 solutions were spin-coated at 1500 rpm for 30 s on substrates. Then, substrates were placed on the hot plate for 30 s, annealing at 70 °C. Next, a mixed solution was prepared by FAI:MAI:MACl (60:6:6 mg) power dissolved in 1 mL of 2-propanol spin-coated on PbI_2 films with a 1500 rpm with a minimum 20 min storage in a nitrogen-filled glove box before annealing. Then, the obtained films were annealed at 150 °C for 15 min under an air atmosphere (relative humidity with 30–40%). A polytetrafluoroethylene (PTFE) filter filtered all precursors before use.

One-Step Fabrication: The perovskite solution was prepared by mixing the powders methylammonium bromide (22.4 mg), lead bromide (73.4 mg), formamidinium iodide (172 mg), and lead iodide (485 mg). Then, 640 μL DMF and 160 μL DMSO or 80 μL N-methyl-2-pyrrolidone (NMP) were added to the mixed powders. The obtained mixture was dissolved and stirred at 25 °C for 30 min. The perovskite precursor was spin-coated on ITO/SnO_2 substrates at 6000 rpm (800 rpm s^{-1}) for 30 s, and 70 μL chlorobenzene was rapidly added into the center of the substrates under a vertical angle and 5 s before ending the spin-coating process, followed by 40 min annealing at 100 °C. A PTFE filter filtered all precursors before use.

The spiro-OMeTAD solution was prepared by mixing 72.3 mg spiro-OMeTAD, 1 mL CB, 17.5 μL Li-TFSI (520 mg mL^{-1}) in acetonitrile, and 28.8 μL 4-*tert*-butylpyridine. A PTFE filter filtered the solution before use. Then, the answer was dynamically spin-coated on top of the perovskite layer with a speed of 3000 rpm for 30 s. Next, all the devices were stored inside a desiccator (relative humidity < 10%) in a dark environment for 12 h before the gold evaporation under a high vacuum (<10^{-6} Pa) with a rate of 0.6 Å s^{-1}. Finally, the devices were measured frequently before reaching the maximum PCE.

Device Characterization: The *J*–*V* curves of two-step fabricated solar cells were tested with a solar simulator (3A class, Enli Tech) under AM 1.5G (100 mW cm^{-2}) illumination with a KG-5 filter standard solar cell (SRC-2020), and the *J*–*V* data were recorded by a digital source meter (Keithley 2401) with 0.1 V s^{-1} scan speed for both reverse and forward scans. Metal masks (aperture area = 0.09506, 1.0036 cm^2) were placed onto small and large area devices, respectively.

The *J*–*V* curves of one-step fabricated solar cells were tested using a Keithley 2611B source meter under the illumination of a class ABA solar simulator (LS0105, Quantum Design) with a light intensity of 100 mW cm^{-2}, which was calibrated with a reference solar cell (KG-5 filter, Fraunhofer ISE019-2015). The solar cells were measured with a voltage step of 10 mV and an integration time of 100 ms. The aperture area was limited by a metal shadow mask (0.079 cm^2) to avoid overestimating the photocurrent.

GIWAXS: In situ GIWAXS data were recorded by a Lambda 750k (X-Spectrum) detector with a pixel size 55 × 55 μm^2, sample-to-detector distance = 186.379 mm and with an energy of 11.7 keV at the Deutsches Elektronen Synchrotron (DESY) at the MiNaXS beamline (P03) of PE-TRA III.[33] The in situ annealing experiment was executed with a heater (DHS1100, Anton-Paar) under a relative humidity of (38 ± 1)%, which was ideal for the annealing process during device fabrication.[30] During the entire 15 min annealing process, 10 frames were captured with a 0.1 s exposure time in the first minute and subsequently 14 frames with a 0.1 s exposure time per minute. Image processing was done with the Python-based DPDAK package.[54] The transformation to *q*-space, intensity corrections for path attenuation, detector absorption, photon polarization, and solid angle for detector images were processed by the Matlab-based

package GIXSGUI.[55] The sample-to-detector distance was first calibrated with LaB$_6$ and CeO$_2$ powders and further calibrated by the ITO peaks as in the previous study.[35] The GIXSGUI package processed Radial cuts for pseudo-XRD analysis and azimuthal cuts for orientation analysis.

SEM: A Zeiss Gemini NVision 40 field emission scanning electron microscope measured the scanning electron images of perovskite films. A voltage of 3 kV was used with a working distance of 2.8 mm for SEM. Contrast, brightness, and color were modified via ImageJ.

External Quantum Efficiency (EQE): The EQE spectra were collected using an EQE system (QE-R 3011, Enli) in DC mode.

Atomic Force Microscopy (AFM): The AFM images were measured by the MFP-3D, Asylum Research, in tapping mode using conical-shaped tips with a radius of 7 nm, and the data were processed through Gwyddion.

Maximum Power Point Tracking: The long-term operational stability was executed under the protocol of ISOS-L-1, the MPPTs of encapsulated (edge sealing by UV curable resin with a glass cover) perovskite solar cells fabricated by type I and type II lead iodide were measured under a solar simulator (ABB class, 94041A, Newport) under AM 1.5 G illumination (100 W cm^{-2}, 25 °C) with calibrated light intensity by a KG-5 filter standard solar cell (#1887, Newport calibrated), and the data were collected for about every 30 min.[56]

The long-term operational stability was executed under the protocol of ISOS-L-2, the MPPTs of encapsulated (edge sealing by UV curable resin with a glass cover) perovskite solar cells fabricated by the lead iodide precursors with different amounts of water were measured under solar simulator with Light-emitting Diode (LED) light sources with an illumination power of 100 W cm^{-2} with calibrated light intensity (1 sun, 55 °C) by a standard silicon solar cell. The data were collected about every 30 min.

Hole-Only and Electron-Only Devices: Hole-only devices were fabricated with the structure of ITO/PTAA/perovskite/PTAA/Au. The 3 mg PTAA was dissolved in 1 mL toluene solution and was deposited on ITO substrates at 6000 rpm for 30 s. Then, the substrates were annealed at 100 °C for 10 min. The perovskite layers were fabricated, as mentioned before. Next, another PTAA layer was fabricated on top of the perovskite layer with 10 min annealing at 100 °C. Finally, 80 nm gold was deposited with a rate of 0.6 Å s^{-1} under the pressure of 10^{-6} Pa.

Electron-only devices were fabricated with ITO/PCBM/perovskite/PCBM/Ag structure. The 20 mg PCBM was dissolved in 1 mL CB solution and was deposited on ITO substrates at 2000 rpm for 30 s. Then, the substrates were annealed at 90 °C for 10 min. When substrates cooled down, the perovskite layers were fabricated, as explained before. Next, another PCBM layer was fabricated on top of the perovskite layer. Finally, 80 nm silver was deposited with a rate of 0.2 Å s^{-1} for 1 nm, 0.4 Å s^{-1} for 5 nm, and 0.6 Å s^{-1} for 74 nm under 10^{-6} Pa pressure.

OPTP Experimental Setup: OPTP spectroscopy was performed as described in a previous publication.[57] Briefly, the samples were placed in a vacuum and photoexcited with 400 nm wavelength laser pulses obtained by frequency doubling the output of amplified, 15 fs pulse duration Ti–Sapphire system (SpectraPhysics: MaiTai-Ascend-Spitfire) with a Beta Barium Borate (BBO) crystal. The transmission of the THz probe (generated with a trilayered, 2 nm W–1.8 nm Co$_{40}$Fe$_{40}$B$_{20}$–2 nm Pt spintronic emitter pumped by an 800 nm wavelength laser pulse obtained from the system described above) was measured by electro-optic sampling in 1 mm thick ZnTe (110) crystal, using a gate beam from the same laser system.[58] The change in the gate's polarization was measured with a quarter-wave plate, polarization-splitting cube, and balanced photodiode detector. The differential THz transmission was measured by modulating the THz generation beam and the photoexcitation beam with optical choppers and acquiring the voltage reading from the balanced photodiode detectors with a custom-made Field Programmable Gate Arrays (FPGA)-based Analog to Digital Converter (ADC) acquisition board designed to replace the need for a boxcar integrator and double lock-in amplifier setup used previously.[59] The time delays between the gate pulse, the THz generation pulse, and the photoexcitation (pump) pulse were controlled with optical delay stages. The pump fluence was adjusted with a neutral density filter wheel to obtain photoexcitation pulse fluence of 25, 20, 12, 6, and 3 μJ cm^{-2} for respective decay traces shown in Figure S15 (Supporting Information).

**ADVANCED
SCIENCE NEWS**

www.advancedsciencenews.com

**ADVANCED
MATERIALS**

www.advmat.de

Absorption Spectrum: The absorption spectrum was measured in a vacuum using a Fourier Transform Infrared Spectroscopy (FTIR) spectrometer (Bruker: Vertex 80v) with a tungsten lamp, CaF_2 beam splitter, Si detector, and reflection–transmission attachment in the sample chamber.

Photoluminescence (PL): The steady-state photoluminescence spectra, as well as time-resolved photoluminescence transients, were recorded by photoexciting the thin films in vacuum with 398 nm wavelength laser pulses from a diode laser (PicoHarp: LDH-D-C-405 M) and collecting the photoluminescence with achromatic lenses into a grating spectrometer (Princeton Instruments: SP-2558). The light reflected from the grating was directed either onto a silicon-intensified charge-coupled device array (Princeton Instruments: PI-MAX4) for steady-state PL spectrum measurement or through a slit (for wavelength selection) and onto a single-photon avalanche diode (SPAD) detector (Micro Photon Device (MPD): PDM series) for TRPL measurement.

The time-resolved PL was measured with the TCSPC technique. In this measurement, the thin film samples were excited with an excitation fluence of 0.77 μJ cm^{-2} at a 125 kHz repetition rate, and the PL was directed onto the SPAD detector, timed by a TCSPC event timer (PicoHarp 300). The PL decay traces were measured at 805 ± 10 nm wavelength (peak of PL), and data were acquired for a relatively short period of 30 s to minimize the effect of light-induced defect formation.[60]

Thermal Admittance Spectroscopy: The TAS measurement was carried out using an electrochemical workstation (Zennium Zahner, Germany) with a frequency of 1 Hz to 3 MHz, and the test temperature was 25 °C.

Drift–Diffusion Simulation: An n–i–p architecture with ITO/SnO_2/perovskite/spiro-OMeTAD/gold was simulated through SCAPS-1D for this study. An AM 1.5G solar spectrum was applied for the whole simulation. All detailed parameters for simulation are shown in Tables S4,S5 (Supporting Information). A batch simulation was executed by modifying the hole (10^{-3} to 10^2 cm^2 V^{-1} s^{-1}) and electron mobility (10^{-3} to 10^2 cm^2 V^{-1} s^{-1}) of the perovskite materials.

Supporting Information

Supporting Information is available from the Wiley Online Library or from the author.

Conflict of Interest

The authors declare no conflict of interest.

Author Contributions

R.G. and Q.X. contributed equally to this work. R.G. and Q.X. conceived the project and devised the experimental framework. Q.X. and P.G. developed the protocols for fabricating the devices. A.U. and L.M.H. conducted experiments involving OPTP spectroscopy, TRPL measurements, and associated analyses. R.G., T.X., J.E.H., A.C., M.S., and S.V.R. performed GI-WAXS measurements using synchrotron-based techniques and handled the subsequent data analysis. Q.X. and T.G. captured SEM images of the samples, while X.J. acquired AFM images of the same. Q.X., Z.D., S.L., and M.Y. provided expertise in MPPT for solar cells. R.G. and S.L. created schematic visualizations. R.G. and Q.X. initiated the initial draft, with P.G. and P.M.-B. overseeing the entire project. All authors actively participated in revising the paper.

Data Availability Statement

The data that support the findings of this study are available in the supplementary material of this article. The raw data can also be found at the following public repository: https://doi.org/10.14459/2023mp1728246.

[1] F. Fu, J. Li, T. C.-J. Yang, H. Liang, A. Faes, Q. Jeangros, C. Ballif, Y. Hou, *Adv. Mater.* **2022**, *34*, 2106540.

[2] Y. Fu, H. Zhu, J. Chen, M. P. Hautzinger, X.-Y. Zhu, S. Jin, *Nat. Rev. Mater.* **2019**, *4*, 169.

[3] Y. Liu, Y. Zhang, X. Zhu, Z. Yang, W. Ke, J. Feng, X. Ren, K. Zhao, M. Liu, M. G. Kanatzidis, S. Liu, *Sci. Adv.* **2021**, *7*, eabc8844.

[4] Z. Li, T. R. Klein, D. H. Kim, M. Yang, J. J. Berry, M. F. A. M. van Hest, K. Zhu, *Nat. Rev. Mater.* **2018**, *3*, 18017.

[5] Best research-cell efficiency chart NREL., **2023** Available at https://www.nrel.gov/pv/cell-efficiency.html.

[6] J. Burschka, N. Pellet, S.-J. Moon, R. Humphry-Baker, P. Gao, M. K. Nazeeruddin, M. Grätzel, *Nature* **2013**, *499*, 316.

[7] N. J. Jeon, J. H. Noh, Y. C. Kim, W. S. Yang, S. Ryu, S. I. Seok, *Nat. Mater.* **2014**, *13*, 897.

[8] N. J. Jeon, J. H. Noh, W. S. Yang, Y. C. Kim, S. Ryu, J. Seo, S. I. Seok, *Nature* **2015**, *517*, 476.

[9] Q. Jiang, Y. Zhao, X. Zhang, X. Yang, Y. Chen, Z. Chu, Q. Ye, X. Li, Z. Yin, J. You, *Nat. Photonics* **2019**, *13*, 460.

[10] J. J. Yoo, G. Seo, M. R. Chua, T. G. Park, Y. Lu, F. Rotermund, Y.-K. Kim, C. S. Moon, N. J. Jeon, J.-P. Correa-Baena, V. Bulovic, S. S. Shin, M. G. Bawendi, J. Seo, *Nature* **2021**, *590*, 587.

[11] A. Wakamiya, M. Endo, T. Sasamori, N. Tokitoh, Y. Ogomi, S. Hayase, Y. Murata, *Chem. Lett.* **2014**, *43*, 711.

[12] M. Matuchova, O. Prochazkova, J. Maixner, K. Zdansky, J. Zavadil, *Phys. Status Solidi C* **2005**, *2*, 1275.

[13] M. Matuchová, K. Žďánský, M. Svatuška, J. Zavadil, O. Procházková, *Chem. Pap.* **2007**, *61*, 36.

[14] R. A. Kerner, E. D. Christensen, S. P. Harvey, J. Messinger, S. N. Habisreutinger, F. Zhang, G. E. Eperon, L. T. Schelhas, K. Zhu, J. J. Berry, D. T. Moore, *ACS Appl. Energy Mater.* **2023**, *6*, 295.

**ADVANCED
SCIENCE NEWS**

www.advancedsciencenews.com

**ADVANCED
MATERIALS**

www.advmat.de

[15] R. A. Kerner, K. Schutt, K. Zhu, J. J. Berry, *ACS Energy Lett.* **2022**, *7*, 4333.

[16] Y. Zhang, S. Seo, S. Y. Lim, Y. Kim, S.-G. Kim, D.-K. Lee, S.-H. Lee, H. Shin, H. Cheong, N.-G. Park, *ACS Energy Lett.* **2020**, *5*, 360.

[17] J. You, Y. Yang, Z. Hong, T.-B. Song, L. Meng, Y. Liu, C. Jiang, H. Zhou, W.-H. Chang, G. Li, Y. Yang, *Appl. Phys. Lett.* **2014**, *105*, 183902.

[18] K. Shoyama, W. Sato, Y. Guo, E. Nakamura, *J. Mater. Chem. A* **2017**, *5*, 23815.

[19] C.-G. Wu, C.-H. Chiang, Z.-L. Tseng, M. K. Nazeeruddin, A. Hagfeldt, M. Grätzel, *Energy Environ. Sci.* **2015**, *8*, 2725.

[20] C.-H. Chiang, M. K. Nazeeruddin, M. Grätzel, C.-G. Wu, *Energy Environ. Sci.* **2017**, *10*, 808.

[21] C. Clegg, I. G. Hill, *RSC Adv.* **2016**, *6*, 52448.

[22] Y.-H. Kye, C.-J. Yu, U.-G. Jong, Y. Chen, A. Walsh, *J. Phys. Chem. Lett.* **2018**, *9*, 2196.

[23] Y. Wu, A. Islam, X. Yang, C. Qin, J. Liu, K. Zhang, W. Peng, L. Han, *Energy Environ. Sci.* **2014**, *7*, 2934.

[24] H.-H. Huang, Z. Ma, J. Strzalka, Y. Ren, K.-F. Lin, L. Wang, H. Zhou, Z. Jiang, W. Chen, *Cell Rep. Phys. Sci.* **2021**, *2*, 4.

[25] K. Liu, Y. Luo, Y. Jin, T. Liu, Y. Liang, L. Yang, P. Song, Z. Liu, C. Tian, L. Xie, Z. Wei, *Nat. Commun.* **2022**, *13*, 4891.

[26] G. E. Eperon, S. N. Habisreutinger, T. Leijtens, B. J. Bruijnaers, J. J. van Franeker, D. W. Dequilettes, S. Pathak, R. J. Sutton, G. Grancini, D. S. Ginger, R. A. J. Janssen, A. Petrozza, H. J. Snaith, *ACS Nano* **2015**, *9*, 9380.

[27] M. K. Gangishetty, R. W. J. Scott, T. L. Kelly, *Nanoscale* **2016**, *8*, 6300.

[28] X. Huang, F. Cheng, B. Wu, N. Zheng, *J. Phys. Chem. Lett.* **2022**, *13*, 1765.

[29] W. S. Yang, J. H. Noh, N. J. Jeon, Y. C. Kim, S. Ryu, J. Seo, S. I. Seok, *Science* **2015**, *348*, 1234.

[30] Y. Zhao, F. Ma, Z. Qu, S. Yu, T. Shen, H.-X. Deng, X. Chu, X. Peng, Y. Yuan, X. Zhang, J. You, *Science* **2022**, *377*, 531.

[31] U.-G. Jong, C.-J. Yu, G.-C. Ri, A. P. Mcmahon, N. M. Harrison, P. R. F. Barnes, A. Walsh, *J. Mater. Chem. A* **2018**, *6*, 1067.

[32] N. N. Intan, J. Pfaendtner, *ACS Nano* **2023**.

[33] A. Buffet, A. Rothkirch, R. Döhrmann, V. Körstgens, M. M. Abul Kashem, J. Perlich, G. Herzog, M. Schwartzkopf, R. Gehrke, P. Müller-Buschbaum, S. V. Roth, *J. Synchrotron Radiat.* **2012**, *19*, 647.

[34] A. Y. Grishko, M. A. Komkova, E. I. Marchenko, A. V. Chumakova, A. B. Tarasov, E. A. Goodilin, A. A. Eliseev, *Nano Res.* **2023**, *16*, 9435.

[35] R. Guo, D. Han, W. Chen, L. Dai, K. Ji, Q. Xiong, S. Li, L. K. Reb, M. A. Scheel, S. Pratap, N. Li, S. Yin, T. Xiao, S. Liang, A. L. Oechsle, C. L. Weindl, M. Schwartzkopf, H. Ebert, P. Gao, K. Wang, M. Yuan, N. C. Greenham, S. D. Stranks, S. V. Roth, R. H. Friend, P. Müller-Buschbaum, *Nat. Energy* **2021**, *6*, 977.

[36] M. A. Reus, L. K. Reb, A. F. Weinzierl, C. L. Weindl, R. Guo, T. Xiao, M. Schwartzkopf, A. Chumakov, S. V. Roth, P. Müller-Buschbaum, *Adv. Opt. Mater.* **2022**, *10*, 2102722.

[37] H. X. Dang, K. Wang, M. Ghasemi, M.-C. Tang, M. De Bastiani, E. Aydin, E. Dauzon, D. Barrit, J. Peng, D.-M. Smilgies, S. De Wolf, A. Amassian, *Joule* **2019**, *3*, 1746.

[38] M. Qin, K. Tse, T.-K. Lau, Y. Li, C.-J. Su, G. Yang, J. Chen, J. Zhu, U.-S. Jeng, G. Li, H. Chen, X. Lu, *Adv. Mater.* **2019**, *31*, 1901284.

[39] A. Wlochowicz, A. Jeziorny, *J. Polym. Sci., Polym. Phys. Ed.* **1972**, *10*, 1407.

[40] M. Ohring, *Engineering Materials Science*, Academic Press, San Diego, CA **1995**.

[41] V. Hinrichs, G. Kalinka, G. Hinrichsen, *J. Macromol. Sci., Part B: Phys.* **1996**, *35*, 295.

[42] B.-W. Park, N. Kedem, M. Kulbak, D. Y. Lee, W. S. Yang, N. J. Jeon, J. Seo, G. Kim, K. J. Kim, T. J. Shin, G. Hodes, D. Cahen, S. I. Seok, *Nat. Commun.* **2018**, *9*, 3301.

[43] X. Y. Liu, *J. Chem. Phys.* **2000**, *112*, 9949.

[44] Y. Y. Kim, E. Y. Park, T.-Y. Yang, J. H. Noh, T. J. Shin, N. J. Jeon, J. Seo, *J. Mater. Chem. A* **2018**, *6*, 12447.

[45] J. S. Renny, L. L. Tomasevich, E. H. Tallmadge, D. B. Collum, *Angew. Chem., Int. Ed.* **2013**, *52*, 11998.

[46] P. Tiwana, P. Parkinson, M. B. Johnston, H. J. Snaith, L. M. Herz, *J. Phys. Chem. C* **2010**, *114*, 1365.

[47] A. M. Ulatowski, A. D. Wright, B. Wenger, L. R. V. Buizza, S. G. Motti, H. J. Eggimann, K. J. Savill, J. Borchert, H. J. Snaith, M. B. Johnston, L. M. Herz, *J. Phys. Chem. Lett.* **2020**, *11*, 3681.

[48] M. Burgelman, K. Decock, S. Khelifi, A. Abass, *Thin Solid Films* **2013**, *535*, 296.

[49] L. M. Herz, *ACS Energy Lett.* **2017**, *2*, 1539.

[50] A. Solanki, M. M. Tavakoli, Q. Xu, S. S. H. Dintakurti, S. S. Lim, A. Bagui, J. V. Hanna, J. Kong, T. C. Sum, *Adv. Mater.* **2020**, *32*, 1907864.

[51] V. M. Le Corre, E. A. Duijnstee, O. El Tambouli, J. M. Ball, H. J. Snaith, J. Lim, L. J. A. Koster, *ACS Energy Lett.* **2021**, *6*, 1087.

[52] D. Neamen, *Semiconductor Physics and Devices*, McGraw-Hill, Inc., New York **2002**.

[53] Y. Shao, Z. Xiao, C. Bi, Y. Yuan, J. Huang, *Nat. Commun.* **2014**, *5*, 5784.

[54] G. Benecke, W. Wagermaier, C. Li, M. Schwartzkopf, G. Flucke, R. Hoerth, I. Zizak, M. Burghammer, E. Metwalli, P. Müller-Buschbaum, M. Trebbin, S. Förster, O. Paris, S. V. Roth, P. Fratzl, *J. Appl. Crystallogr.* **2014**, *47*, 1797.

[55] Z. Jiang, *J. Appl. Crystallogr.* **2015**, *48*, 917.

[56] M. V. Khenkin, E. A. Katz, A. Abate, G. Bardizza, J. J. Berry, C. Brabec, F. Brunetti, V. Bulovic, Q. Burlingame, A. Di Carlo, R. Cheacharoen, Y.-B. Cheng, A. Colsmann, S. Cros, K. Domanski, M. Dusza, C. J. Fell, S. R. Forrest, Y. Galagan, D. Di Girolamo, M. Grätzel, A. Hagfeldt, E. von Hauff, H. Hoppe, J. Kettle, H. Köbler, M. S. Leite, S. Liu, Y.-L. Loo, J. M. Luther, et al., *Nat. Energy* **2020**, *5*, 35.

[57] C. Wehrenfennig, G. E. Eperon, M. B. Johnston, H. J. Snaith, L. M. Herz, *Adv. Mater.* **2014**, *26*, 1584.

[58] T. Seifert, S. Jaiswal, U. Martens, J. Hannegan, L. Braun, P. Maldonado, F. Freimuth, A. Kronenberg, J. Henrizi, I. Radu, E. Beaurepaire, Y. Mokrousov, P. M. Oppeneer, M. Jourdan, G. Jakob, D. Turchinovich, L. M. Hayden, M. Wolf, M. Münzenberg, M. Kläui, T. Kampfrath, *Nat. Photonics* **2016**, *10*, 483.

[59] C. L. Davies, J. Borchert, C. Q. Xia, R. L. Milot, H. Kraus, M. B. Johnston, L. M. Herz, *J. Phys. Chem. Lett.* **2018**, *9*, 4502.

[60] S. G. Motti, M. Gandini, A. J. Barker, J. M. Ball, A. R. Srimath Kandada, A. Petrozza, *ACS Energy Lett.* **2016**, *1*, 726.

2310237 (10 of 10)